



ELSEVIER

Contents lists available at ScienceDirect

Icarus

journal homepage: www.elsevier.com/locate/icarus

Understanding the water cycle above the north polar cap on Mars using MRO CRISM retrievals of water vapor

Alain S.J. Khayat^{a,b,*}, Michael D. Smith^a, Scott D. Guzewich^a

^a NASA Goddard Space Flight Center, Greenbelt, MD 20771, United States

^b Center for Research and Exploration in Space Science & Technology (CRESSST II), Department of Astronomy, University of Maryland, College Park, MD 20742, United States

ABSTRACT

The north polar cap (NPC) on Mars is the major reservoir of atmospheric water (H₂O) currently on Mars. The retrieval and monitoring of atmospheric water vapor abundance are crucial for tracking the cycle of water above the NPC. The Compact Reconnaissance Imaging Spectrometer for Mars (CRISM) aboard the Mars Reconnaissance Orbiter (MRO) has provided a wealth of data that extend over 5 + Martian years, covering the time period between 2006 and 2016. CRISM is ideally suited for spring and summer observations of the north polar region (latitudes poleward of 60 °N). The retrievals of water vapor column abundances over this extended period of time were performed over both ice-free and water ice covered surfaces, extending the coverage of the water vapor maps to include the permanent cap, where a maximum value of 90 precipitable micrometers (pr- μ m) is retrieved, as compared to 60 pr- μ m over ice-free regions in the North Polar Region. Away from summertime maximum, modest interannual variability in the water vapor abundance is observed. Zonal averages over all the observed Martian years combined show a developing water front that shifts northward towards summer, before dissipating over the permanent cap during mid-summer. A prominent feature at latitudes around 75 °N shows large abundances of water vapor, indicating a water vapor annulus encircling the retreating edge of the seasonal polar cap during late spring. Meridional transport of water modeled here show that the annulus may be a result of the convergence of water vapor from both south and north along the retreating edge of the NPC.

1. Introduction

One of the most fascinating aspects that makes Mars the focus of intense scientific interest is the possibility that life could have evolved there during its past. Water is essential to life, and in all its physical states, it depends on the climate. Thus, water is a powerful indicator for sensing global climate changes on the planet, and crucial for understanding the processes that can affect its climate, on short and long time scales.

The behavior and evolution of water on the planet are deeply connected to the rates of exchange between the different reservoirs on the planet, whether the polar caps, the atmosphere, the regolith, the surface frost or ice clouds (Pankine et al., 2009). The north polar cap (hereafter, NPC) is the main reservoir of atmospheric water on Mars, and yet little is known about the water cycle above it.

On an annual scale, along with the major cycles of carbon dioxide (CO₂) and dust, the water cycle controls the current climate of Mars (e.g., Smith, 2002). On timescales on the order of thousands of years in the variations of the orbital obliquity of Mars, alternating layers of ice and dust were formed within the polar ice deposits as a response to the incremental transport of water and dust to or from the polar regions during each Mars year (Jakosky and Haberle, 1992).

The north polar cap on Mars consists of water ice and smaller amounts of CO₂ ice and dust. At the beginning of the northern spring season, the CO₂ ice, which is on top, sublimates first, gradually exposing the water ice of the permanent north polar cap (hereafter, permanent cap) to interact with the atmosphere at increasing rates spanning the late northern spring and early summer seasons. As the largest known reservoir of water on the planet in the current epoch, the NPC is the major source of atmospheric water during northern summer, which is subsequently transported to the equatorial latitudes by the end of the summer season (e.g., Haberle and Jakosky, 1990). The NPC continues to contribute to the water cycle on Mars by the sublimation and deposition processes of water during the northern spring/summer, and autumn/fall seasons, respectively (Hvidberg and Zwally, 2003).

The retrievals and monitoring of water vapor above the NPC are crucial for tracking the cycling of water between the surface and the atmosphere of Mars. The importance of monitoring water vapor abundances and their spatial and temporal variation is to understand the non-uniformity of water sublimation across the north polar cap, and to look for interannual dependences. This helps to enable the identification of sources and sinks of water vapor in the cap. In addition, it opens a window into the evolution of the cap in terms of its shrinkage or growth over long timescales. The results from such surveys are

* Corresponding author at: Solar System Exploration Division, Mailstop 693, NASA Goddard Space Flight Center, Greenbelt, MD 20771, United States
E-mail address: alain.khayat@nasa.gov (A.S.J. Khayat).

<https://doi.org/10.1016/j.icarus.2018.12.024>

Received 18 June 2018; Received in revised form 13 November 2018; Accepted 6 December 2018

Available online 08 December 2018

0019-1035/© 2018 Elsevier Inc. All rights reserved.

fundamental for developing and validating water sublimation models above the NPC on Mars, such are the ones by Haberle and Jakosky (1990) and Hvidberg and Zwally (2003).

Previous retrievals of water vapor from orbiters around Mars included using the Mars Atmospheric Water Detector (MAWD) onboard the Viking Orbiter. Davies (1982) observed the north polar region (latitudes 60°N to 90°N) during northern spring and summer in 1977 and 1978, corresponding to Mars Year (MY) 13. MY represents the Mars year number, where MY1 begins at the northern spring equinox on April 11, 1955 (Clancy et al., 2000). The presented polar maps covered latitudes higher than 45°N to the pole, with a spatial resolution of 2°–3° in latitude. Water vapor results from the MAWD observations show amounts in excess of 100 precipitable microns (pr- μm ; equivalent to the liquid water thickness if the water over the entire atmosphere condenses onto the surface of the planet) at regions surrounding the permanent cap, at $L_s = 110^\circ$, presenting a great deal of structure in the water vapor distribution. Davies (1982) found structure in the water vapor distribution in the longitudinal direction around the NPC, with a factor of 2 difference at the same latitude.

Three decades later, using the Mars Global Surveyor (MGS) Thermal Emission Spectrometer (TES; Christensen et al., 1992), Pankine et al. (2009, 2010) produced water vapor abundance maps in Mars' north polar regions during spring and summer seasons after averaging the data in boxes of 2° latitude, 4° longitude and 5° in L_s . The data were obtained from several sparse observations during MY24 (1999), MY25 (2000–2001), MY26 (2002–2003) and MY27 (2004). Comparative results between the TES and MAWD results suggest the presence of a discontinuity in the release of water vapor from localized source (“outbursts”) in areas near the permanent cap ($\sim 75^\circ\text{N}$). The formation of these short-lived (< 10 sol) outbursts could be explained by a combination of mechanisms including rapidly varying water ice sublimation rates, and changes in the magnitude and direction of surface winds, but direct correlation has not been yet demonstrated. TES and MAWD retrievals share broad similarities, including the timing of the maximum water vapor abundances during the summer time around $L_s = 105^\circ\text{--}115^\circ$, and the low abundances in the winter hemisphere. However, for the same location and season ($L_s \sim 90^\circ\text{--}135^\circ$), the water abundance levels retrieved using MAWD are twice as great as those retrieved using TES data. Pankine et al. (2009) suggested that the source of water is likely the permanent cap, because of the difference in nature between MAWD's observations that were able to cover the permanent cap, and the TES retrievals that were not able to so.

Pankine et al. (2010) later reported updated retrievals of water vapor over the polar regions including the seasonal frost and the permanent ice cap (surface temperature < 220 K). The peak abundances over the permanent cap were observed between $L_s = 90^\circ$ and 110° in MY25 and $L_s = 90^\circ$ and 130° in MY 26, and reached 80 ± 15 pr- μm . During MY24, the peak timing of $L_s = 115^\circ$ is consistent with Jakosky and Farmer (1982), and Smith (2002).

Fedorova et al. (2010) revisited the global MAWD data and implemented updated spectroscopic parameters for water (HITRAN 2004 and later, Rothman et al. 2005, 2009), as well as improved atmospheric model from the Mars Climate Database (Forget et al., 1999). The reported retrievals indicate a twofold decrease in the total water vapor abundances in all seasons and at most of the observed geographic locations as compared to the original retrievals by Jakosky and Farmer (1982).

On the global scale, there is a long history of observations of water vapor over the atmosphere that started in the 1970s, obtained by the Viking/MAWD that covered the planet for 1.5 Mars years (Jakosky and Farmer 1982). Because of its importance in terms of understanding the Martian climate, there is a semi-continuous monitoring of atmospheric water vapor since the late 1990s. The measurements relied on instruments onboard spacecraft, such as TES on MGS (Smith, 2002, 2004), Compact Reconnaissance Imaging Spectrometer for Mars (CRISM) aboard the Mars Reconnaissance Orbiter (MRO) (Smith et al., 2009,

2018; Toigo et al., 2013), Observatoire pour la Minéralogie, l'Eau, les Glaces et l'Activité (OMEGA) (Melchiorri et al., 2007, 2011), Spectroscopy for Investigation of Characteristics of the Atmosphere of Mars (SPICAM) and Planetary Fourier Spectrometer (PFS) on Mars Express (Fedorova et al., 2006; Fouchet et al., 2007; Trokhimovskiy et al., 2015).

The retrievals of water vapor (Smith et al., 2009, 2018; Toigo et al., 2013) using CRISM observations used large spatial averages and focused on the global, seasonal trends. They both explicitly excluded observations that contained spectral signatures of surface ice.

The results returned from the different observations share general conclusions that the year-to-year seasonal cycle of water vapor is more or less stable. However, in some regions, at the same season, there are significant year-to-year differences, such as in the aftermath of the global dust storm of MY 28 (2007) (e.g., Smith et al., 2018). In another case, Pankine et al. (2010) noted the presence of a polar annulus around the NPC, exhibiting interannual water vapor abundance variabilities during the northern spring and summer times. These variabilities could likely be due to a change in the polar circulation, local dust storms, or a change in the thermal structure above the NPC. The water cycle over the polar cap is therefore deeply connected with the global cycle and cannot be separated from it.

In Section 2, we describe the CRISM instrument, the observations used in this work, the morphology of the CRISM spectrum, and we present the seasonal distribution of the surface ice over the NPR. In Section 3 we provide details about the improved version of the radiative transfer model that for the first time makes possible the retrievals of atmospheric water vapor at near-infrared wavelength over surface ice. We show synthetic spectra with the retrieved quantities, and discuss the uncertainties in the retrievals. The retrieval results and the meridional transport of water vapor are presented and discussed in Section 4, and we finally summarize our findings in Section 5.

2. Data Set: Spacecraft, instrument and observations

2.1. CRISM instrument

The Mars Reconnaissance Orbiter (MRO) has been making observations since November 2006. The spacecraft operates at low-altitude, in a near-circular, near-polar, and a Sun-synchronous orbit at mean local solar times 03:00 and 15:00 (Zurek and Smrekar, 2007). A key objective of the Compact Reconnaissance Imaging Spectrometer for Mars (CRISM) on MRO (Murchie et al., 2007) is “atmospheric monitoring to characterize the spatial and temporal properties of the atmosphere for the studies of climate, weather and photochemistry”. CRISM is a hyperspectral imager with spatial resolution on Mars that can reach 15 m/pixel, with two detectors that cover visible (362 nm–1056 nm) and near-infrared (1001–3920 nm) wavelengths. Each detector is composed of 640 pixels in the spatial direction and 480 pixels in the spectral direction.

CRISM's two surface tracking observing configurations allow “targeted” (different emission angles and longer integration time) and “push-broom” (nadir) modes for targeted and mapping observations on Mars, respectively. The “hyperspectral” mode covers 545 channels and operates at the full instrument's spectral resolving power $R = \lambda/\Delta\lambda \sim 150$ at 2300 nm, a spectral resolution of ~ 15 nm and a spectral sampling of 6.55 nm, whereas the “multispectral” mode returns a subset of channels (72 channels). The multispectral mapping observations allow moderate resolutions of 100–200 m, and cover a larger area than the targeted observations. Such observations are very well suited for tracking the global cycling of water between the surface and the atmosphere at different seasons.

2.2. CRISM observations over the NPC

CRISM is a near-infrared reflectance spectrometer, observing the

planet through solar reflected radiation, and therefore it is well suited for spring and summer observations of the north polar region, including the NPC and the permanent cap. At such wavelengths, the polar regions cannot be observed during polar autumn and winter when they are not illuminated by the sun. The observations were chosen with solar incidence angles below 80° . In addition, in every targeted observation, we selected the CRISM images with the lowest emission angle around nadir. In contrast, the frequency of the observations does not allow time-resolved measurements in the window of days to weeks (Smith et al., 2018).

In order to avoid the small variation of wavelength as a function of column number across the image (also known as the “spectral smile”), and to reduce the uncertainty in the water vapor abundance, we bin the central 100×100 pixels of each CRISM image. The spatial pixel averaging covers an area of 2×2 km at each observation over the NPC. The same image processing techniques have been presented in Smith et al. (2009, 2018).

The CRISM observations used in this study extend over 5 + Mars years, from MY 28 at $L_s = 112^\circ$, to MY 33 at $L_s = 86^\circ$, corresponding to September 27, 2006 and September 29, 2016, respectively. These 34,500 + targeted observations include ~5300 observations at latitudes higher than 60° N (Fig. 1). The limited lifetime of CRISM’s cry-cooler resulted in a more careful operation planning, leading into an ongoing reduction in the number of observations with time in order to extend the use of the operating cooling mechanism (Smith et al., 2018).

2.3. Morphology of a CRISM spectrum

Fig. 2 represents two typical hyperspectral spectra as returned by CRISM. Each spectrum (I/F) is obtained by dividing the radiance (I) at CRISM by the solar irradiance (F) incident at the top of the Martian atmosphere at the time of the observation, which leaves the spectral features belonging to the surface of Mars and its atmosphere.

The top panel in Fig. 2 represents a near-nadir Emission Phase Function (EPF) CRISM spectrum with no surface ice, taken at 69° N, 320° W longitude and during mid-summer season ($L_s = 119^\circ$), at a 100×100 spatial average. In the spectrum, atmospheric CO_2 absorption bands are present around 1500 nm and 2000 nm. Water vapor major atmospheric bands are around 1360 nm, 1900 nm and 2600 nm. Weak absorptions from carbon monoxide gas (CO) show up at 2350 nm.

The spectrum in the bottom panel is from a near-nadir FRT CRISM image, taken over the polar cap at 85.4° N during early spring season. Surface ice features originating from CO_2 and H_2O appear in this spectrum. Individual contributions from surface ice have been separated and are shown with an offset in I/F for clarity. The reflectance spectrum of CO_2 ice (in blue) shows absorptions features roughly at 1400 nm, 1600 nm, 2300 nm and strong ones around 2000 nm and 2600 nm. H_2O ice reflectance (in red) reveals major absorptions around 1500 nm, 2000 nm and 2700 nm.

The water vapor band at 2600 nm is the strongest among the four principal water vapor bands, and therefore it was utilized in previous works (Melchiorri et al., 2007; Smith et al., 2009, 2018; Maltagliati et al., 2011) to provide reliable water abundance retrievals. However, in the current work, we extend the retrievals over the polar regions covered by surface ice. Fig. 2 shows that the water vapor band at 2600 nm is heavily affected by the deep CO_2 and water ice spectral signatures, which make the atmospheric water vapor retrievals almost impossible to reliably obtain. In addition, the water vapor bands around 1900 nm and 2600 nm are mixed with atmospheric carbon dioxide signatures, as well as water/carbon dioxide ice signatures when the surface ice is present. On the other hand, the water vapor band at 1368 nm, even-though weaker than that at 2600 nm, is not influenced by any atmospheric features belonging to carbon dioxide, and not fully mixed with surface ice features belonging to H_2O or CO_2 .

Using CRISM spectra, we define a water vapor band index at

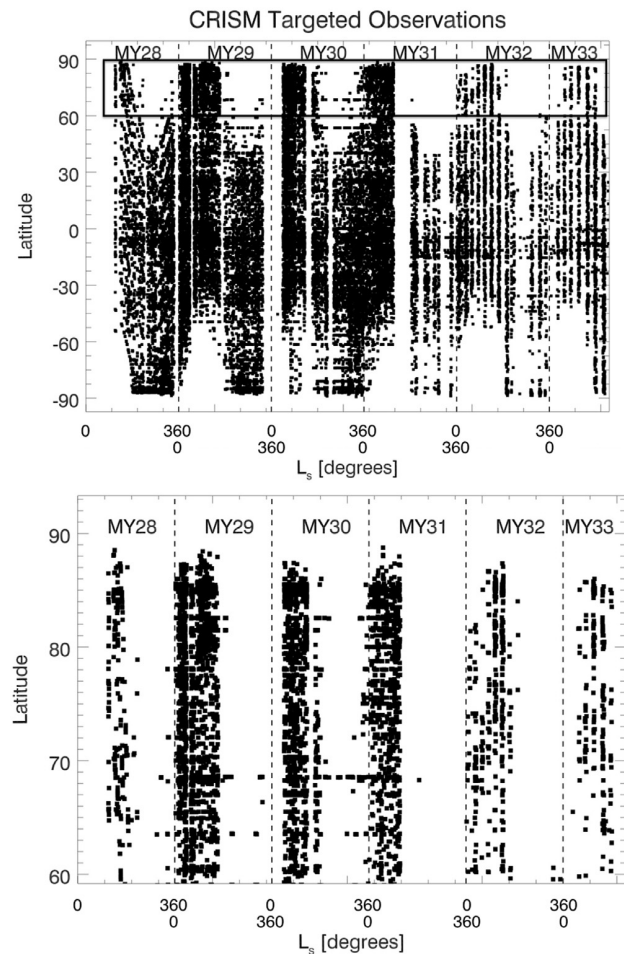


Fig. 1. The seasonal (L_s) and latitudinal distribution of the CRISM observations used in this work. The top panel represents the CRISM targeted observations across the Martian globe, whereas the bottom panel represents a subset of the targeted observations, over latitudes higher than 60° N. $L_s = 0^\circ$ – 360° corresponds to one Mars Year (MY). The gaps near the winter poles are due to the limitations on the solar incidence angle. We made use of the observations over the NPC from the bottom panel to characterize the water cycle over the polar cap, and to link them to the global observations from the top panel to measure the meridional water transport between the NPC and lower latitudes.

1368 nm as H_2O water index at 1368 nm = $1 - \frac{IF(1368)}{IF(1329)^{0.5}IF(1414)^{0.5}}$. The index is a metric for the depth of the water vapor band. Using the current hyperspectral CRISM observations, we map the seasonal dependence of the water vapor index and present it in Fig. 3. The map clearly illustrates the atmospheric water cycle on Mars as described in Smith et al. 2009, showing large differences in the hemispheric and seasonal behavior of water vapor. The strong north-to-south gradient in water vapor abundance is well depicted, showing a low-latitude summer maximum ($L_s = 290^\circ$ – 300°) that is notably weaker than the high-latitude summer maximum around $L_s = 120^\circ$ (see Fig. 8 in Smith et al., 2009). The asymmetry in water vapor abundance is attributed to the larger amounts of water vapor that are released from the NPC, the main reservoir of atmospheric water, as compared to the ‘drier’ southern polar cap that is mostly covered with CO_2 ice all year long and is working as a cold trap, therefore inhibiting water sublimation (Smith 2008; Maltagliati et al., 2011). As a result, the water vapor at ~ 1360 nm is a better metric for retrieving water vapor abundances over the ice, after modifying the radiative transfer model to accommodate for surface ice (see Section 3.2).

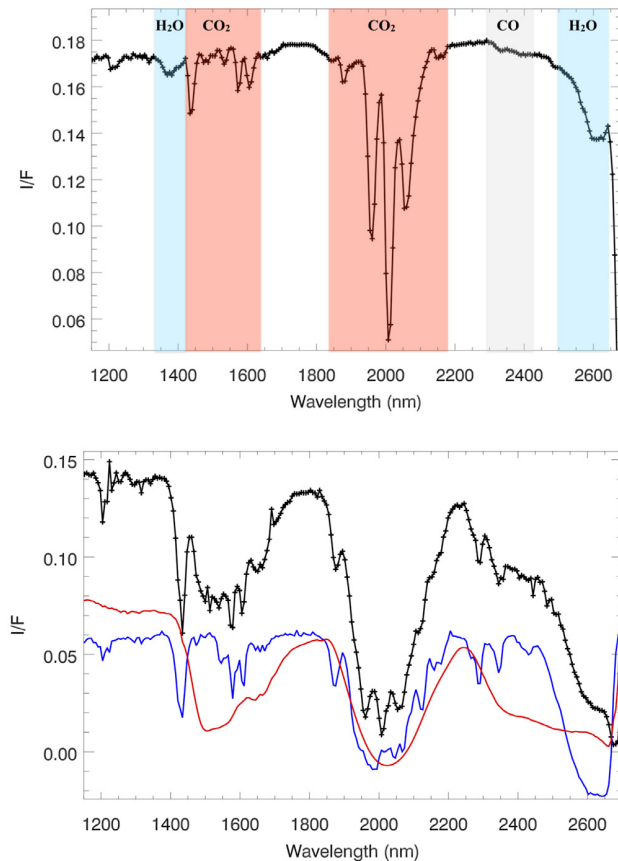


Fig. 2. Upper panel: CRISM spectrum (black) of the hyperspectral observation EPF0000C3BA taken at $L_s = 119^\circ$, 69° N latitude, and 320° W longitude. The main atmospheric absorption bands of CO₂, H₂O and CO are highlighted in red, blue and grey, respectively. Lower panel: The CRISM hyperspectral spectrum (black) FRT00009CEA at $L_s = 28^\circ$, 85° N latitude, and 179° W longitude. The individual surface ice reflectance spectra (offset for clarity) of the CO₂ and H₂O are shown here in blue and red, respectively. Both spectral signatures originating from the surface ice contribute to the CRISM spectrum in black as shown in this figure. No absorption feature of atmospheric H₂O is prominent around 1368 nm because the atmosphere is dry above this latitude at this time during early northern spring since the sublimation of water did not initiate yet. (For interpretation of the references to color in this figure legend, the reader is referred to the web version of this article.)

2.4. Surface ice distribution

Solar reflected radiation by icy surfaces contains spectral signatures that are characteristic of the ice. The surface ice band depth is a good indicator of the surface ice properties, including the abundance, the grain size and the granular mixture (Appéré et al., 2011). Using CRISM's hyperspectral data over the NPR, we calculated ice absorption band depths for CO₂ and H₂O at 2344 nm and 1500 nm respectively using the following equations: H_2O ice index = $1 - \frac{IF(1500)}{IF(1385)^{0.7} IF(1772)^{0.3}}$ (Langevin et al., 2007; Appéré et al., 2011) and CO_2 ice index = $1 - \frac{IF(2344)}{0.5 \times IF(2318) + 0.5 \times IF(2371)}$ (Viviano-Beck et al., 2014). where $IF(\lambda)$ indicates the reflectance at the wavelength λ , in nm. The ice index increases with grain size and the amount of surface ice. The threshold values for the presence of water and carbon dioxide CO₂ ice are 0.1 and 0.045 for the ice indices, respectively. These threshold values were chosen by calculating the CO₂ and H₂O ice indices when the depths of the respective ice bands are at 3 standard deviations ($3 \sigma_{rms}$) away from the continuum. Using the CRISM data from 5 + Mars years, we were able to detect the presence of surface CO₂ and water ice and plot their geographic and seasonal dependence (Fig. 4).

During the months of autumn and winter, the north polar regions are covered by a layer of CO₂ ice (10 cm to 1 m thick). At the beginning of northern spring, solar radiation illuminates the north polar regions, therefore heating up the surface to temperatures higher than 148 K, leading to the sublimation of CO₂ ice which gradually recedes poleward (Fig. 4- top panel). The seasonal layer of CO₂ ice shrinks as spring progresses, until it completely disappears at the beginning of summer at $\sim L_s = 75^\circ$ as indicated. The disappearance of the CO₂ ice layer gradually reveals the presence of the water ice from the permanent ice cap (Fig. 4- bottom panel), which remains visible until the recondensation of atmospheric CO₂ at the beginning of the northern fall equinox.

3. Radiative transfer

Radiative transfer models in planetary atmospheres such as Mars enable the retrieval of the physical state of the planet and its atmosphere. In the thermal infrared and longer wavelength regimes (i.e., submillimeter), the emergent flux from Mars is dominated by the thermal emission from the planet and its atmosphere, and the radiative transfer models depend on the thermal contrast between the surface and the atmosphere of the planet (e.g., Khayat et al., 2015, 2017). In contrast, at the CRISM near-IR (hereafter, near IR) wavelengths, solar radiation is dominant with a two-way airmass between the Sun and Mars' surface and then from Mars' surface to the spacecraft. The quantities involved in modeling synthetic spectra are the following: the viewing geometry, the surface albedo, temperature and pressure at the surface of Mars, the thermal structure of its atmosphere, the intrinsic spectral parameters (broadening coefficients, line strengths) of the atmospheric gases, and the absorption and scattering from suspended aerosols (dust and water ice particles). At the operating wavelengths of CRISM, the contribution from aerosol scattering becomes dominant compared with absorption.

The retrieval assumptions follow those described in Smith et al. (2009, 2018). The Mars heliocentric distance, the solar incidence and emission angles are extracted from spacecraft records. The surface temperature, pressure and the atmospheric temperature structure are estimated from previous retrievals (Smith, 2004) using the Mars Global Surveyor's Thermal Emission Spectrometer (MGS/TES). In previous works (Smith et al., 2009, 2018), the surface pressure was retrieved from the atmospheric CO₂ absorption band around 2350 nm, but in the current one, the presence of strong spectral features originating from surface ices over polar regions compromises the retrievals around the atmospheric CO₂ band, so instead surface pressure is taken from model results.

In order to handle the large number of CRISM spectra and speed up the spectral modeling while conserving the fidelity of the retrieval process, we applied the correlated-k distribution method for gas absorptions (Lacis and Oinas, 1991). The water vapor is assumed to be well-mixed (constant volume mixing ratio) below the water condensation level, and non-existent above it. Maltagliati et al. (2013) conducted solar occultations observations of the Martian atmosphere using the SPICAM spectrometer onboard Mars Express in order to infer the vertical distribution of water vapor. They indicated the presence of supersaturation in some observations during northern spring-summer. However, our retrieved water vapor column abundances are generally not significantly affected by this amount of supersaturation. The spectral line parameters used were obtained from the HITRAN 2012 database (Rothman et al., 2013). We adopted the solar spectrum from MODTRAN (Berk et al., 1998).

The presence of aerosols affects the gas absorption depths, and therefore need to be accounted for in the retrieval process. The seasonal and latitudinal aerosol optical depth are obtained from concurrent Mars Odyssey THEMIS observations (Smith et al., 2009), and sampled at the locations and seasons of the CRISM observations. The spectral dependence of the aerosol opacity depends on the particle size distribution, the effective radius (r_{eff}), the vertical abundance, and the index of

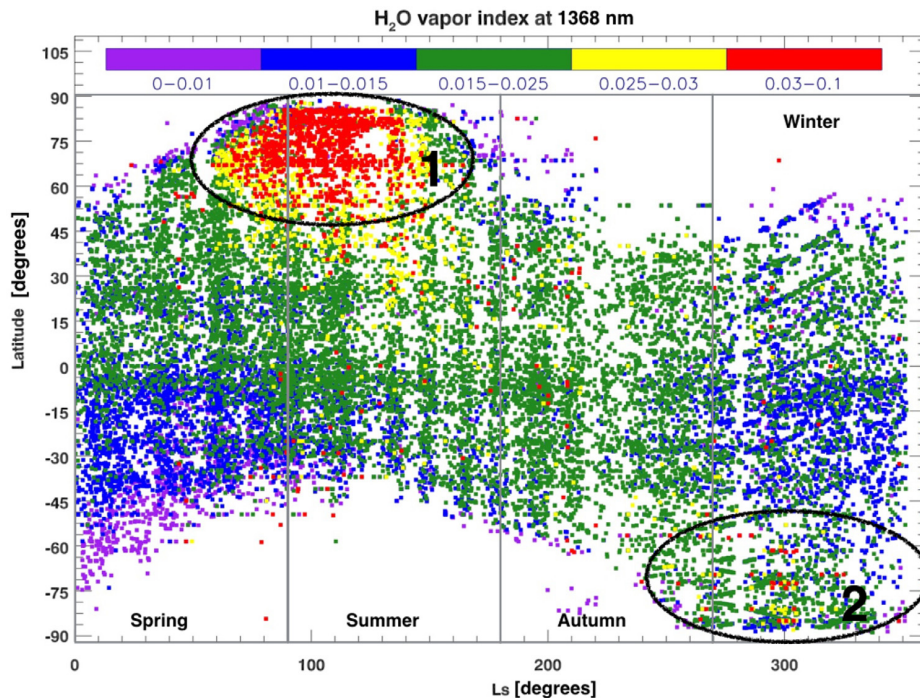


Fig. 3. The analysis using all CRISM hyperspectral observations reveals the seasonal dependence of the water vapor index at 1368 nm. The index is unitless, and it is a metric for the water vapor band depth, where higher index indicates more water vapor. The vertical lines represent the boundaries between the different seasons. As observed, the annual cycle of water with its distinctive seasonal and geographical behavior is very well depicted here. The asymmetry in the maxima of water vapor abundance between the two polar summers is also clearly observed here, as indicated in regions 1 and 2 inside the black contours.

refraction. The particle sizes that are used in this work, $r_{\text{eff}} = 2 \mu\text{m}$ and $1.5 \mu\text{m}$ for water ice and dust respectively, were taken from modeling TES spectra (Wolff and Clancy, 2003) and from comparing TES, mini-tes and CRISM spectra (Clancy et al., 2003; Wolff et al., 2006, 2009). Errors in the values of the aerosol opacities do not lead to significant uncertainties in the water vapor retrievals, and are sufficient for the purpose of this work (see Section 3.4). The water ice is considered to be well mixed above the condensation level, and dust is considered to be well mixed with the background gas (Smith et al., 2009, 2018). Scattering from aerosol is treated using the discrete ordinates method described in Thomas and Stamnes (1999). The aerosol scattering properties were obtained from processing Emission Phase Function (EPF) targeted observations. The CRISM EPF observations have the advantage of taking spectra of the same spot on Mars at 11 emission angles (1 at nadir and 10 at inbound and outbound emission angles between 30° and 70°), therefore allowing the extraction of the scattering properties of aerosols (Wolff et al., 2009).

3.1. Retrieval process

The retrieval process is iterative, and the first step is to define the continuum around the water vapor band at 1360 nm in the observed CRISM spectrum. The water band extends over 15 CRISM spectral channels between 1329 nm and 1421 nm. At first we find the effective Lambert albedo of the surface at these wavelengths, then linearly interpolate inside the band, without making any interpretation related to the mineralogy of the surface (Smith et al., 2009). This step is essential in establishing the contrast between the continuum and the center of the water vapor band, and therefore for retrieving the water abundance. Previously (Smith et al., 2009, 2018), the surface pressure was retrieved at each observation from fitting the “triplet” structure of the band CO_2 around 2000 nm. In the current work, the presence of surface ice affects the carbon dioxide absorption band, making it impossible to retrieve the surface pressure. As a result, the surface pressure is computed from a model using the known seasonal dependence of surface pressure from landers (e.g., Tillman and Guest, 1987) and a correction for altitude which is read from an elevation map generated by MOLA (Smith, et al., 2001). As mentioned above, aerosol extinction (scattering

and absorption) is included in the retrieval process, and the fundamental idea is to vary the water vapor abundances until a best fit is achieved between the modeled and the observed spectrum as returned by CRISM. During each retrieval, the height of the water condensation level is retrieved from the water vapor abundance in an iterative manner. The height of the condensation level is derived from the water vapor column abundance and the atmospheric temperature profile as extracted from the TES climatology. The output quantities from the retrieval process are the water vapor column abundance, the height of the condensation level, and the equivalent Lambert albedo as a function of wavelength between the two continuum points of the water vapor band.

3.2. Treatment of surface ice

As shown in Fig. 2, the wide spectral absorption around 1500 nm belonging to water ice on the surface of Mars affects the channels on the longward side of the water vapor band centered at ~ 1360 nm. Therefore, not correcting for the presence of surface ice compromises the retrievals over the polar regions, where most of the water vapor is originating from.

The treatment of water ice occurs in two stages. First, the continuum at 1421 nm is corrected for, and next, the channels that are affected by the presence of surface ice are excluded from the fit. We analyzed ~ 1100 CRISM spectra with no surface ice at latitudes above 60°N , and measured the continuum levels (I/F) at 1329 nm and 1421 nm. The scatter plot shown in Fig. 5 obtained from plotting the continuum levels against each other reveals a strong correlation, with a Pearson correlation coefficient of 0.9998, and a linear fit of $IF(1421 \text{ nm}) = 1.003025 \times IF(1329 \text{ nm}) - 0.00043$. The number of channels in the water vapor band that are affected by the surface ice depends on the width and depth of the surface ice feature at 1500 nm. In the extreme case where the surface is covered with large ice grain sizes and at high concentrations, only nine out of fifteen channels that make up the water vapor absorption band remain unaffected by the surface ice. These unaffected channels are on the short wavelength portion of the water vapor band between 1329 and 1382 nm. We modified the radiative transfer model to accommodate using only the

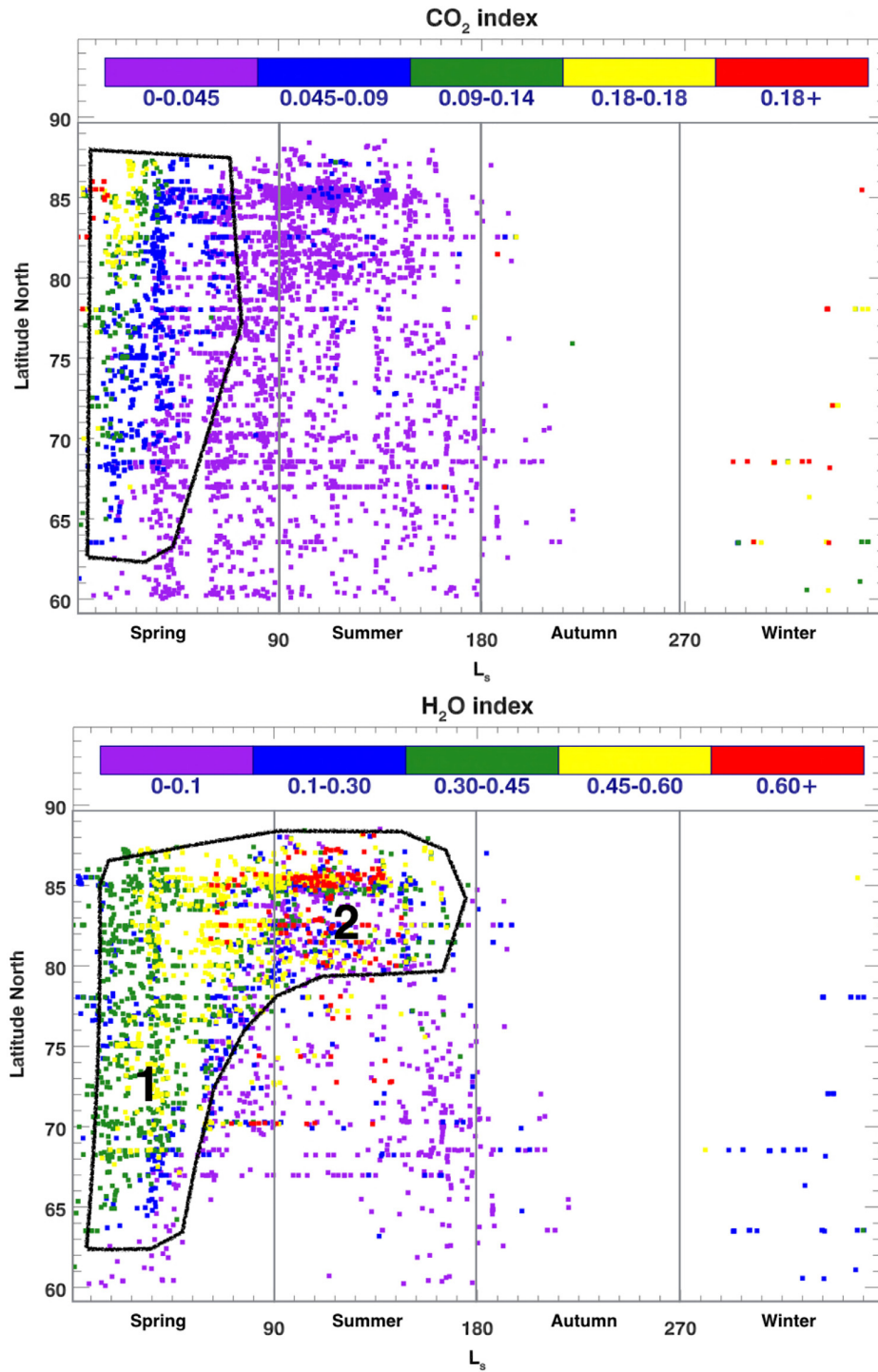


Fig. 4. Analysis of the CRISM spectra over all the Mars years reveals the presence of surface water and CO₂ ice signatures by measuring their respective ice indices. The index is unitless, and higher ice index indicates more surface ice/larger grain sizes. The plots show the seasonal variations of the ice indices from the NPC. The vertical lines separate between different seasons. The top panel shows the gradual disappearance of CO₂ ice as spring progresses, until its complete disappearance at L_s = 75° around the end of northern spring, gradually exposing the surface water ice beneath it (bottom panel). The contour in black represents the geographic latitudes on Mars covered by CO₂ ice. The lower panel indicates the progression of surface H₂O ice poleward as the CO₂ ice spectral features recede. Region 1 in the contour in black represents the exposed surface water ice after the seasonal layer of CO₂ ice shrinks due to the sublimation of CO₂. Region 2 in the contour represents the permanent water ice cap, fully exposed during northern summer. Our analysis clearly depicts the sublimation and part of the recondensation cycle of the water and CO₂ using CRISM spectra.

unaffected channels in the water vapor band by implementing a weighting factor in the calculation of the Chi-squared fitting parameter that excludes the compromised spectral channels, in the following equation: $\chi^2 = \frac{\sum_{i=1}^{10} [w_i \times r_i]}{\sum_{i=1}^{10} [w_i]}$; where χ^2 is the Chi-squared of the fitting, $r_i = (o_i - m_i)^2$ is the squared difference between the observed o_i and the modeled spectrum m_i at channel i , and w_i is the weighting factor for each channel. $w_i = 1$ for the first seven channels between 1329 nm and 1369 nm, $w_i = 0.3$ and 0.1 for the 8th and 9th channels at 1375 nm and 1382 nm respectively, and $w_i = 1$ for 10th channel at 1421 nm.

Using the same ~1100 CRISM spectra with no surface ice, we

applied this modified version of the radiative transfer code, and compared the retrievals results to those returned from the radiative transfer code described in Smith et al. (2009, 2018), which uses the water vapor band at 2600 nm. The results are plotted against each other in Fig. 6. A high linear correlation ($R = 0.931$) is found. We use the linear relationship $pr - \mu m(1360 \text{ nm}) = 0.95 \times pr - \mu m(2600 \text{ nm}) + 0.94$ to normalize between the water vapor retrievals at 1360 nm and 2600 nm.

Fig. 4 shows that at the beginning of northern spring, part of the polar regions is still covered with CO₂ ice. The surface (~145 K) acts as a cold trap for the water vapor in the atmosphere, making it a dry polar

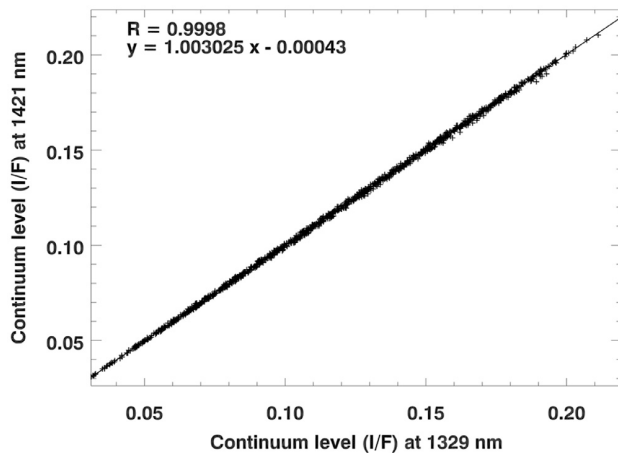


Fig. 5. The scatter plot obtained by plotting the continuum levels at 1421 nm against those at 1329, by using ~ 1100 CRISM spectra with no surface ice, at latitudes above 60°N . The Pearson correlation coefficient found is ~ 1 .

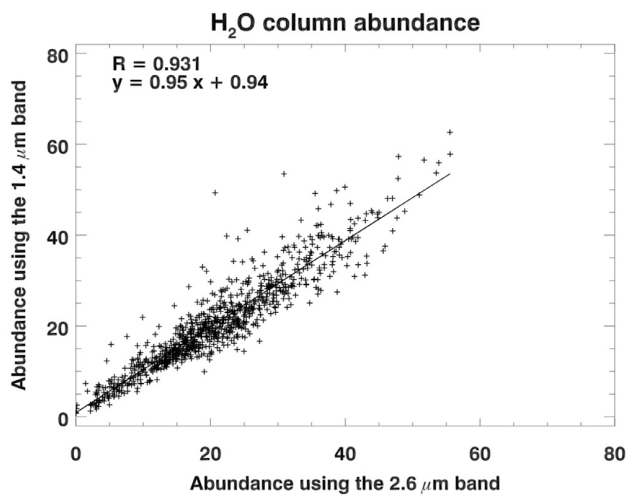


Fig. 6. The scatter plot obtained by plotting the retrieved water vapor abundances using the modified version of the radiative transfer model that relies on the water vapor band at 1360 nm and which uses weighting factors, against the retrievals from using the water vapor band at 2600 nm. The Pearson correlation coefficient found is 0.93.

atmosphere (Haberle et al., 2017). We therefore excluded observations taken over CO₂ ice ($< 2\%$ of the total) since the water sublimation process has not yet begun at that time of the season.

3.3. Synthetic spectra

In order to avoid the presence of systematics that arise from using different retrieval codes, we applied the same code described in Section 3 over all the CRISM spectra, regardless whether the surface is covered with ice or not. In Fig. 7 we present the result from fitting a synthetic spectrum to the observed one of EPF0000C3BA, in the absence of surface ice. The spectrum is observed at $L_s = 119^\circ$, over latitude 69°N and longitude 320°W . The modeled surface pressure is 7.5 mbar and the retrieved water vapor column abundance is 39 $\text{pr-}\mu\text{m}$. The bottom panel shows the result from fitting the atmospheric water vapor band while avoiding the spectral channels that are affected by surface ice in the CRISM observation FRT0000ABD0 taken at 330°W longitude, 77°N latitude, and during northern spring at $L_s = 69^\circ$. The synthetic spectrum in the top panel well depicts the atmospheric water vapor and carbon dioxide at the time of the observations. The retrieved

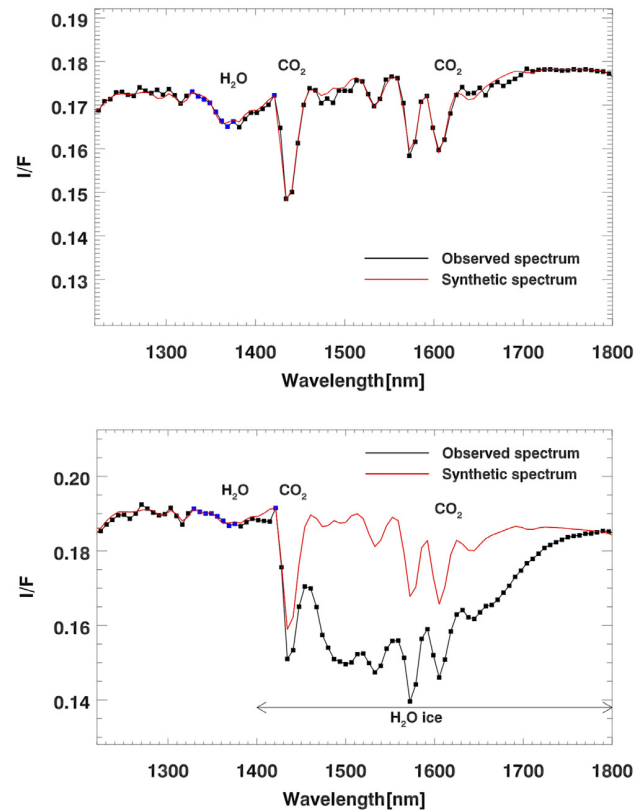


Fig. 7. Upper panel: The best fit spectrum (red) compared against the CRISM observation (black) EPF0000C3BA. This spatially-averaged, near-nadir observation is taken during northern summer at $L_s = 119^\circ$ over an ice-free surface. The retrieved atmospheric water vapor column abundance is 39 $\text{pr-}\mu\text{m}$. Lower panel: The portion of the CRISM spectrum of FRT0000ABD0 as observed over surface ice. The H₂O surface ice band is indicated between 1400 nm and 1800 nm. The best fit spectrum (red) of the atmospheric water and CO₂ is compared against the CRISM observation (black) taken during northern spring at $L_s = 69^\circ$, and the retrieved value for the atmospheric water abundance is 9 $\text{pr-}\mu\text{m}$. In both panels, the channels used in computing the fit of the water vapor band around 1360 nm are shown in blue. (For interpretation of the references to color in this figure legend, the reader is referred to the web version of this article.)

water vapor abundance is 9 $\text{pr-}\mu\text{m}$ with a modeled surface pressure of 8.9 mbar. In both panels, the channels that are used in the fitting process are indicated in blue.

3.4. Uncertainties

The retrieval code used here is a modified version of the one used Smith et al., (2009; 2018). The new algorithm allows retrievals of water vapor at 1360 nm in observations that contain the spectral signatures of surface water ice. Similar retrieval assumptions are made for both the old and new retrieval versions, therefore leading to similar uncertainties in the retrieval results, with an additional uncertainty originating from normalizing between the retrievals at 1360 nm to the retrievals at 2600 nm in Smith et al. (2009, 2018).

The major sources of uncertainty arise from using the HITRAN database to model the spectral bands of water, the use of TES climatology to extract the atmospheric temperature profile, as well as from normalizing between retrievals at 1360 nm to the retrievals at 2600 nm. In addition, uncertainty arises from estimating the continuum level around the water vapor band, using concurrent THEMIS observations to get the atmospheric opacities, and from applying model-related assumptions.

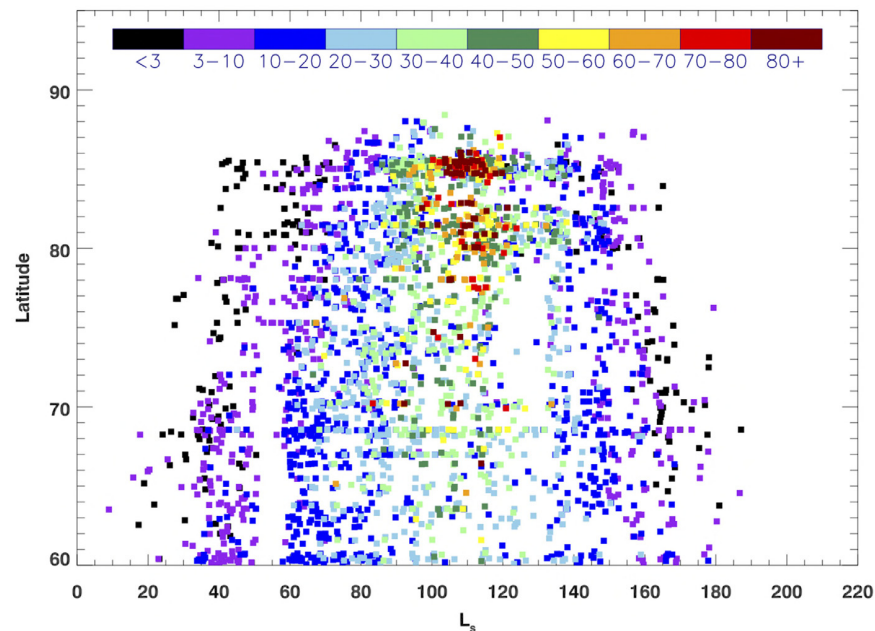


Fig. 8. The variation of the atmospheric water vapor column abundance (pr- μm) during northern spring and summer as a function of latitude from the combined Mars Years (MY 28 to MY 33), as retrieved from ~ 2700 CRISM spectra taken over the north polar region.

The uncertainties in the retrieved results are described in detail in Smith et al. (2009, 2018) and are based on the results of numerical experiments varying different assumptions to determine the related uncertainty in retrieved water vapor abundance. The atmospheric temperature of Mars at the time of the observation affects the temperature-dependent broadening coefficients and line strengths of the water vapor band. Smith (2004) estimated the uncertainty on the temperature profiles to be within 10 K, which leads to an uncertainty of 15% in the retrieved water vapor abundance. The water vapor saturation level is also affected by the atmospheric temperature, and numerical tests applied to the water vapor profile in the data show that changes in the profile lead to a maximum difference of 10% in the retrieved water vapor column abundance.

The broadening coefficients for water vapor depend on the collisional environment in which H_2O exists. The atmosphere of Mars is CO_2 -dominated (95%), but the HITRAN database provides broadening coefficient in an Earth-like atmosphere (mostly nitrogen and oxygen). For simplicity, we multiply the foreign-broadened coefficient of H_2O by 1.5 and apply it to Mars. We chose the representative value of 1.5 in order to be able to make a direct comparison with previous water vapor measurements such as the ones returned by TES (Smith, 2002, 2004) and CRISM (Smith et al., 2009, 2018). It is difficult to estimate the uncertainty arising when making such assumption, but it is not more than 20% in the retrieved water vapor column abundance for any realistic value of the broadening coefficients.

Fig. 6 shows the scatter between the retrieved water vapor column abundance when using the water vapor band at 1360 nm against that at 2600 nm. The uncertainty originating from normalizing values between the two bands is computed by measuring the scatter between the measurements (data) and the fitted line (model) to the data in Fig. 6, which is 23%.

Another assumption made in the retrieval is using concurrent THEMIS aerosol opacity instead of the same CRISM observation to determine the opacities. In the seasons without large dust storms, doubling the aerosol opacity affects the resulting H_2O abundance by 1%. At the time of major dust storms, the dust doesn't allow the measurement of the water abundance all the way down to the surface. Such retrievals with dust optical depths at CRISM wavelengths that are

greater than unity were excluded.

The assumptions made in the radiative transfer model are similar to those described in Smith et al. (2009, 2018), and are related to the number of stratified layers in the Martian atmosphere, the number of levels in the discrete ordinates method, and the polynomial degree expansion which replicates the scattering phase function. Changes in these parameters lead to an uncertainty in the water vapor abundance within 2%.

The 15% and 20% uncertainties given by Smith et al. (2009, 2018) for the individual retrievals arising from the temperature profiles and the broadening coefficients, respectively, are conservative figures. In practice, the vast majority of the time, the actual uncertainty is significantly less than 15% and 20%. The above-mentioned sources of uncertainty are not fully random. We have found through numerical experimentation that there is a correlation between the temperature profiles, the temperature and pressure broadened spectral profiles, and the temperature-dependent (imbedded in the spectral line strength) uncertainty originating from normalizing values between the water vapor band at 1360 nm and that at 2600 nm. In addition, co-adding the retrievals in the spatial and temporal dimensions to reproduce the general behavior of water vapor provides an improvement in the uncertainty as compared to the above-mentioned uncertainty arising from individual retrievals. We therefore estimate the total uncertainty of the retrieved water vapor column abundance to be 25%. We have consistently applied the same assumptions throughout the entire dataset to improve the fidelity of the retrievals in reproducing the seasonal and geographic behavior of water vapor.

4. Results and discussion

For this study, we have obtained successful retrievals for ~ 2700 CRISM nadir-viewing CRISM hyperspectral observations over the NPR. We reject the results where the RMS in the residuals between the observed and synthetic spectra is high and exclude retrievals at observations where the solar incidence angle is higher than 80° (Smith et al., 2009, 2018). A total 37% of these retrievals are for observations over regions covered with surface H_2O ice.

The resulting water vapor column abundance as a function of season

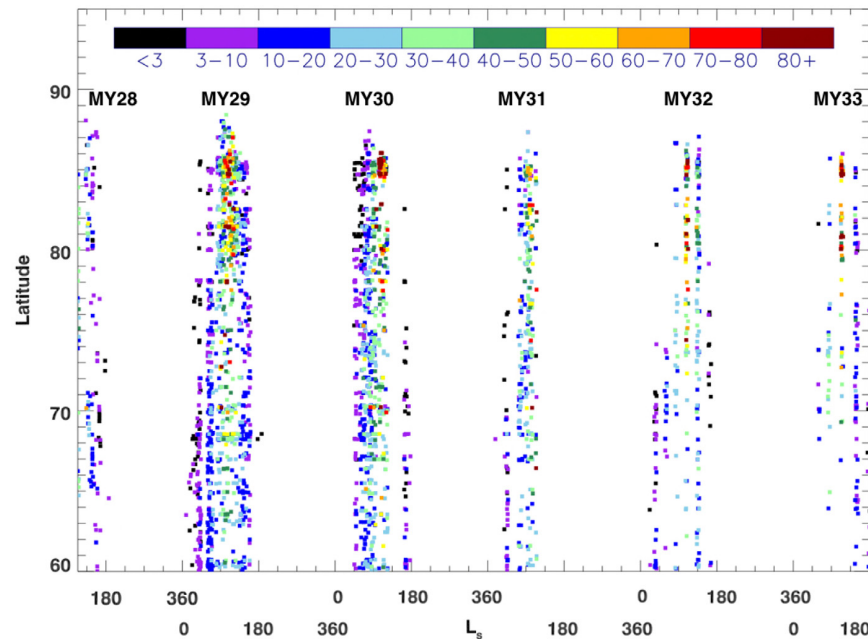


Fig. 9. The seasonal and latitudinal dependence of the atmospheric water vapor abundance (pr- μm) for Mars Years 28, 29, 30, 31, 32 and 33, all put next to each other for comparison, as observed by CRISM. $L_s = 0^\circ\text{--}90^\circ$ represents spring, and $L_s = 90^\circ\text{--}180^\circ$ represents summer of every Martian year.

(L_s) and latitude, which span more than five Mars years (MY 28–MY 33) is shown in Fig. 8. At the beginning of northern spring, the atmosphere above the polar region is dry, and the increasing intensity of the solar insolation drives the water sublimation. Atmospheric water abundance gradually increases until it reaches maximum values above 60 pr- μm at latitudes higher than 77°N between $L_s = 90^\circ$ and 120° during the summertime maximum of water vapor. Later on, the water vapor is transported equatorward, and by $L_s = 180^\circ$ at the end of the water deposition period at high latitudes, the water abundance decreases to levels below 10 pr- μm .

Fig. 9 shows the retrievals from the CRISM observations over the north polar region for individual years since CRISM started returning data (MY 28). MY 29 and MY 30 have the most complete seasonal and spatial coverage. The frequency of the observations in later Mars Years decreased because of the degradation in CRISM's cryo-cooler, and the vertical gaps between the Mars years are due to polar winter. The water cycle over the polar region is clearly depicted between one year and the other.

The long baseline in the CRISM observations with a consistent retrieval algorithm allows the search for interannual variations in the water vapor abundances. The latitudinally-averaged ($60^\circ\text{N}\text{--}87^\circ\text{N}$) water vapor column abundance as a function of season as observed during each Mars years is shown in Fig. 10. The results are zonally averaged by calculating the median values over all latitudes of the NPR, and binned over 10° in L_s . Each zonal average is calculated using hundreds of CRISM observations that are well distributed in longitude, so that there is no bias related to the variation in topography (and other quantities) as a function of longitude.

The top panel of Fig. 10 represents the retrieval results over ice-free surfaces. They exhibit a gradual increase in the water vapor abundance during northern spring, reaching a maximum in each year during early northern summer between $L_s = 100^\circ$ and 120° , and then a gradual decrease with abundances falling below 10 pr- μm after $L_s = 150^\circ$.

The middle panel of Fig. 10 shows the results from the retrievals over the regions covered with water ice. The general trend of water vapor is similar between the retrievals over different surfaces, but lower values of water vapor are observed during early spring, followed by a sharp increase in the water vapor column abundances over the ice-

covered regions. The retrievals over ice-covered surfaces are at higher latitudes compared to those over ice-free surfaces (see Fig. 3, lower panel). During early spring, high-latitude ice-covered regions receive lower solar insolation than the ice-free lower latitude regions, which explains the lower water vapor abundance levels before $L_s = 70^\circ$. Later during early summer, ice-covered regions exhibit rapid sublimation, resulting in water vapor reaching peak values (90 ± 22 pr- μm) over the newly exposed water ice from the permanent cap. As expected, the highest water vapor column abundances at the summertime maximum occur over the ice-covered regions, when compared to the ice-free regions in the top panel. Later during the water deposition period ($L_s = \sim 130^\circ\text{--}170^\circ$), a rapid decrease in the water vapor column abundance is noticeable.

The lower panel of Fig. 10 shows the combined retrievals over both types of surfaces. For most of the observed years, the onset of the water sublimation occurs around $L_s = 30^\circ$, whereas the peak of the summertime maximum occurs between $L_s = 110^\circ$ and 120° for all the observed years, and earlier between $L_s = 100^\circ$ and 110° for MY 30. The maximum column abundance values are different between the Mars years around the summertime maximum, with the interannual difference reaching a factor of 1.5 between MY 29 (70 ± 17 pr- μm) and MY 32 (45 ± 10 pr- μm). At other times of the season between $L_s = 40^\circ$ and $L_s = 90^\circ$ during spring, $L_s = 140^\circ$ and $L_s = 180^\circ$ during summer, no prominent interannual variations in the water vapor abundances are observed within the 25% uncertainty.

Fig. 11 shows the seasonal variation of the water vapor abundance for the 5 + Mars years for 3 different latitude bands. The plots clearly show the delay in the onset timing of the water sublimation as a function of season for increasing latitude. In addition, the plots show that the increase in the water sublimation gets sharper at higher latitude. In the high latitude regions, the water vapor column abundance maxima occur where water ice is covering the surface. Such levels of water vapor around the summertime maximum in the $80^\circ\text{N}\text{--}90^\circ\text{N}$ latitude band can reach 80 pr- μm , twice the levels retrieved in the $60^\circ\text{N}\text{--}70^\circ\text{N}$ latitude bin. Except for MY 30 at high latitudes, the summertime maxima in the 3 different latitude bins occur in the range $L_s = 110^\circ\text{--}120^\circ$. It is interesting to note that there are larger variations in the water vapor abundance between the different Mars years during

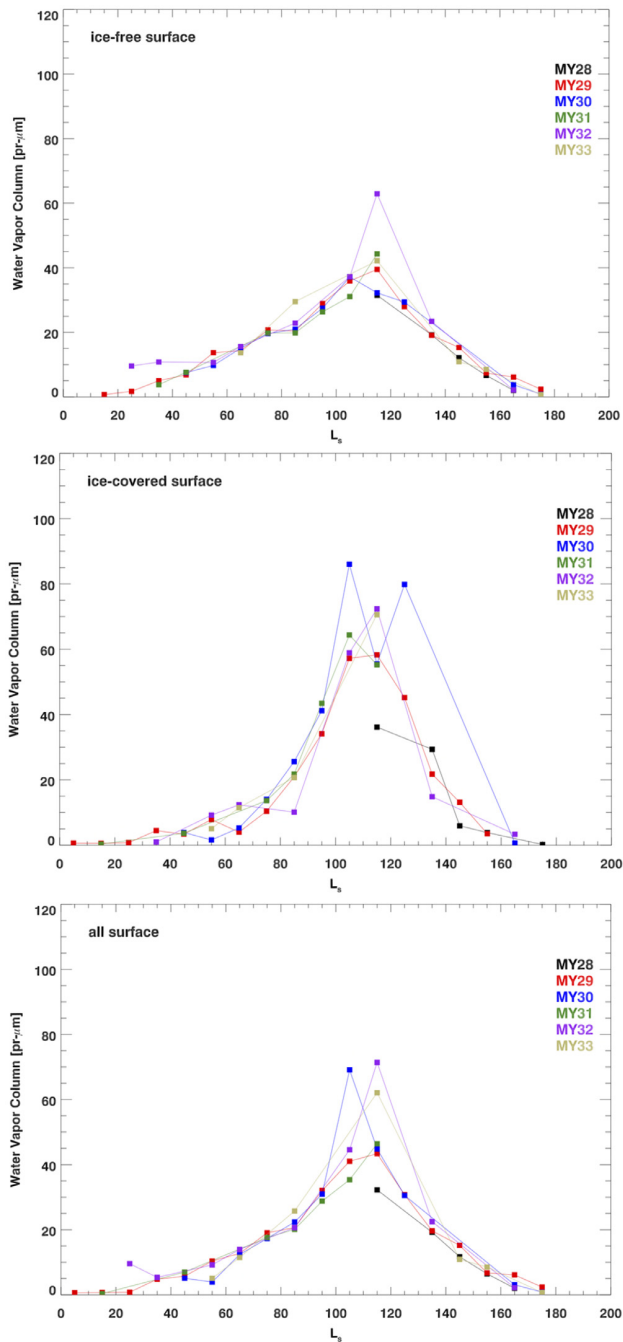


Fig. 10. Latitudinally averaged (60°N – 87°N) atmospheric water vapor column abundance ($\text{pr-}\mu\text{m}$) over the north polar region during northern spring and summer for the 5 + Martian years as observed by CRISM. The top panel represents the retrievals over ice-free surfaces. The middle panel represents the retrievals over surfaces that are covered with water ice, and the lower panel represents the combined retrievals over the north polar region, for both surfaces.

the decay period in the highest latitude bin as compared to the lower latitude bins.

Fig. 12 shows the zonally-averaged water vapor column abundance as a function of latitude and season, with a 2° latitude bin and a 10° bin in L_s . To provide best spatial coverage and to depict the general behavior of water vapor, we show the combined results from all the Martian years between MY 28 and MY 33. The left panel shows the evolution of the water vapor column abundance during spring

($L_s = 0^{\circ}$ – 90°), whereas the right one covers the summer season ($L_s = 90^{\circ}$ – 180°), and all the way to $L_s = 200^{\circ}$. At the beginning of spring, the atmosphere is dry until $\sim L_s = 30^{\circ}$ when the water vapor abundance rises above $5 \text{ pr-}\mu\text{m}$ and keeps increasing until it reaches a maximum of $\sim 65 \text{ pr-}\mu\text{m}$. A developing water vapor front occurs at $L_s = 30^{\circ}$ around 60°N and shifts northward as a function of season. The front reaches its maximum intensity around 83°N before it dissipates above the permanent cap, and then it shifts to lower latitudes, indicating an equatorward transport of water vapor (see Section 4.1 on the meridional transport of water vapor).

A prominent feature in spring between $L_s = 60^{\circ}$ and 70° (in blue) shows large levels of water vapor abundance. This feature indicates a water vapor annulus encircling the retreating edge of the seasonal polar cap during spring at latitudes below 75°N . The same water vapor annulus was also reported by Pankine et al. (2010). The source of water in the annulus is attributed to the water frost existing on top of the CO_2 ice, as well as the newly exposed water frost from the ground as the CO_2 from the retreating edge of the cap sublimates.

Brown et al. (2016) provided insights on the summer cycle over the polar cap by tracking the depths of the H_2O ice absorption feature in the CRISM observations at a region centered at 45°E , 85°N . Brown et al. identified a net sublimation period caused by high solar insolation ($L_s = 90^{\circ}$ – 125°), followed by a net condensation period ($L_s = 125^{\circ}$ – 167°). Fig. 4 in this work clearly depicts the timings for the sublimation of CO_2 and H_2O ices and the deposition of H_2O by using ice indices from both molecules as described in Section 2.4. Additionally, our water vapor retrievals in Figs. 8–12 indicate within 10° of L_s similar onset timings for both the net sublimation and condensation periods presented in Brown et al. (2016). In contrast, water vapor abundances presented in this work cover the entire north polar region, and depict the seasonal behavior of the water vapor for 5 + Martian years.

Pankine et al. (2009) analyzed Viking/MAWD and MGS/TES datasets of water vapor over the north polar region, covering parts of the spring-summer seasons for MY 12 to MY 14 for MAWD, and MY 24 to MY 27 for TES. The MAWD retrievals showed twice as much water vapor (maximum of $80 \text{ pr-}\mu\text{m}$) during the $L_s = 80^{\circ}$ – 140° period as compared to the TES retrievals (maximum of $45 \text{ pr-}\mu\text{m}$) (see Fig. 3 in Pankine et al., (2009)). The high values from MAWD may be attributed to the vapor sublimation from the permanent cap. The thermal infrared measurements from TES rely on the thermal contrast between the surface and the atmosphere, and the retrieval algorithm presented in Pankine et al. (2009) defined a surface temperature cutoff of $T_s > 220 \text{ K}$, therefore disabling retrievals over the permanent cap. In contrast, near-IR observations from MAWD are not surface temperature dependent, and therefore covered the permanent cap where higher sublimation could occur. This could explain the discrepancy between the two results. Interestingly, Fig. 10 in this work shows the retrieval results over ice-free surfaces (top panel), and the water vapor behavior over such surfaces is consistent with the Pankine et al. (2009) TES results. In contrast, between $L_s = 90^{\circ}$ – 130° the retrieval results over the surfaces covered with ice (middle panel) are consistent with the MAWD results. Our improved water vapor algorithm that allows the retrievals over ice-covered surfaces provides a more accurate depiction of the water cycle over the entire NPR.

The twofold decrease in the revisited MAWD water vapor abundance during the polar maximum shown in Fedorova et al. (2010) is attributed to a combination between a larger 1360 nm water vapor band strength and lower water vapor saturation levels around summer polar maximum. However, the retrievals could be biased due to neglecting the contribution from aerosol (atmospheric water ice and dust). More importantly, the polar measurements that are affected by the surface ice absorption feature around 1500 nm were not accounted for. Correct retrievals of water vapor over the permanent cap cannot be obtained without taking into account the presence of surface ice, in particular when addressing the discrepancy between previous retrieval results around summer maximum.

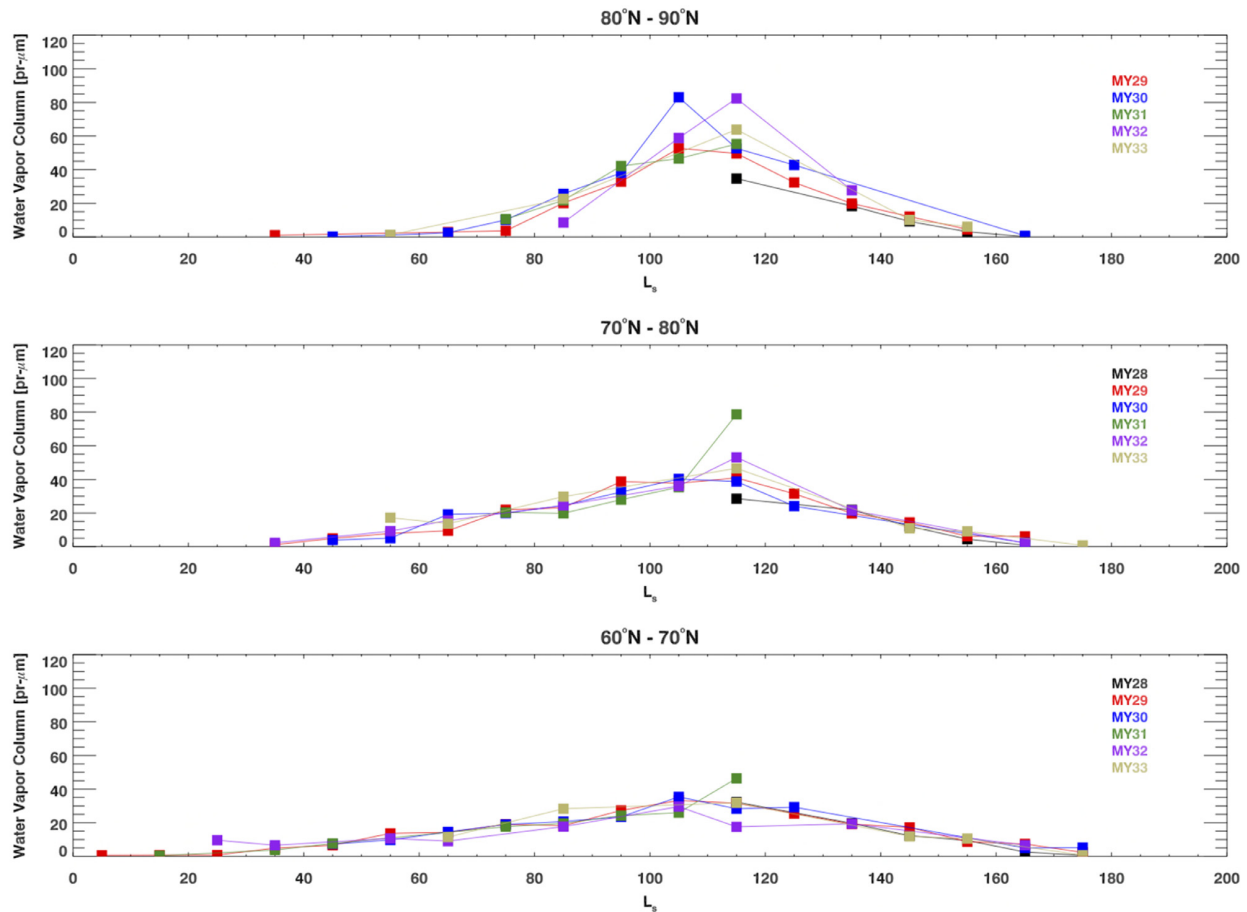


Fig. 11. The seasonal evolution of the atmospheric water vapor column abundance ($\text{pr-}\mu\text{m}$) in three different latitude bands in the north polar region, for the Martian years as observed by CRISM. The different colors represent the different Martian years.

Pankine et al. (2010) revisited the retrieval algorithm and improved it in order to accommodate surfaces with $T_s < 220$ K, therefore covering larger portions of the permanent cap, and presented longitudinal averages of TES water vapor column abundance for 4 Mars years (MY 24–27). The highest abundances (80 ± 15 $\text{pr-}\mu\text{m}$) were observed over the permanent cap during summertime between $L_s = 90^\circ - 110^\circ$ in MY 25, and they extended to $L_s = 130^\circ$ in MY 26. Our zonal averages show high abundances (70 ± 17 $\text{pr-}\mu\text{m}$) between $L_s = 100^\circ - 120^\circ$ when combining results from all the observed Mars years combined. The updated work of Pankine et al. (2010) that covers the permanent cap shows more consistency with the results presented in this work throughout the spring-summer season, in particular around the summertime maximum over the permanent cap.

Additional CRISM water vapor results (Smith et al., 2009, 2018; Toigo et al., 2013) did not include retrievals from observations over surface ice, and therefore presented average water vapor values reaching a maximum of 50 $\text{pr-}\mu\text{m}$ at high northern latitudes, less than the maximum values retrieved in this work. However, Trokhimovskiy et al. (2015) presented SPICAM retrievals of water vapor using the 1360 nm band that accounted for aerosol scattering in contrast to Fedorova et al. (2010), and provided global retrievals for MY 27 to MY 31, showing peak values of 70 $\text{pr-}\mu\text{m}$ over the NPR during the summertime maximum. There was no mention of any accounting for surface ice over the permanent cap where higher values of water vapor column abundance are expected.

4.1. Meridional transport of water vapor

The meridional transport of the water vapor sublimated from the NPC is an important factor in the modern Martian climate. That water, for example, helps produce the distinctive Aphelion Cloud Belt at lower latitudes (Smith, 2004). The CRISM retrievals alone cannot provide information on the water vapor transport, as it is the dynamical fields (i.e., the wind field) that move mass through the atmosphere. Following Montmessin et al. (2017) the meridional transport of water vapor, q , is calculated by multiplying it by the meridional component of the wind vector, v , and taking the zonal average \overline{qv} .

We assume water vapor is well-mixed up to the condensation level (as computed in the retrieval) and use a mass-weighted column mean meridional velocity from the surface to that condensation level in the calculation. The meridional velocity is output from a MarsWRF general circulation model (GCM) simulation run at 5° horizontal resolution in latitude and longitude using a prescribed dust distribution (Montmessin et al., 2004; Toigo et al., 2012). A general description of the MarsWRF GCM is provided by Toigo et al. (2012). Model wind velocity was interpolated to the locations of CRISM retrievals in latitude and longitude. The wind velocity was not decomposed into mean flow and eddy-driven components due to the limited number of the CRISM retrievals available and thus the wind velocity used represents the total of all components of the flow (see Montmessin et al., 2017, for an example of such a decomposition). After calculating the meridional water vapor transport for each CRISM retrieval using MarsWRF meridional wind speeds, the resulting values were zonally averaged and averaged over specific seasonal dates (L_s).

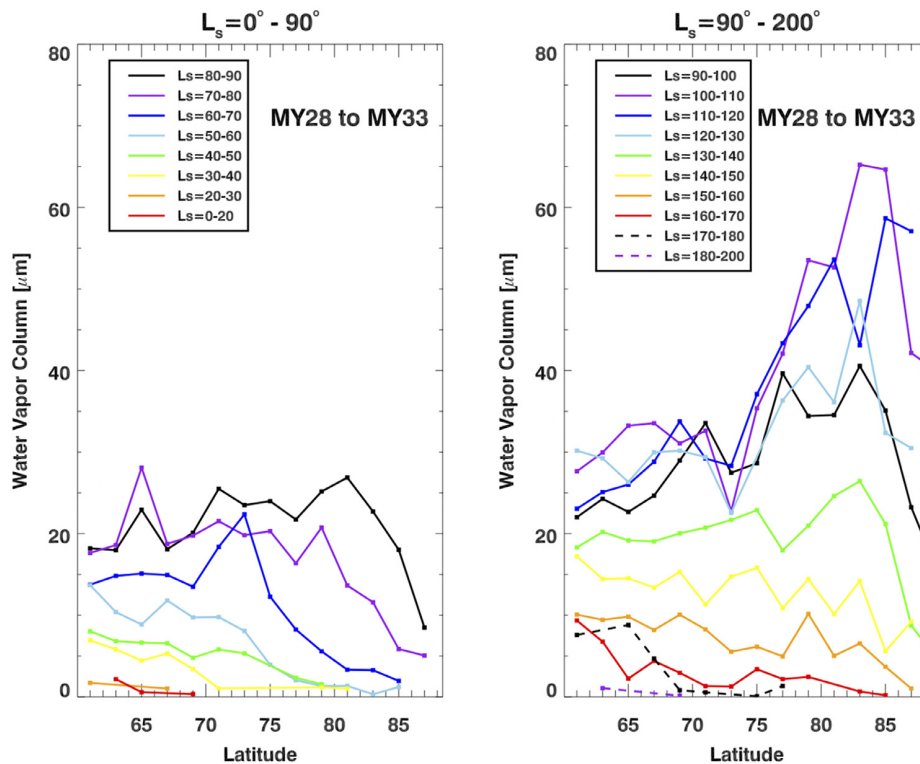


Fig. 12. The evolution of the zonally-averaged CRISM water vapor column abundance (pr- μm) for the combined 5 + Martian years during northern spring and summer between $L_s = 0^\circ$ and 200° . The retrievals are presented in bins of 2° latitude, and 10° in L_s .

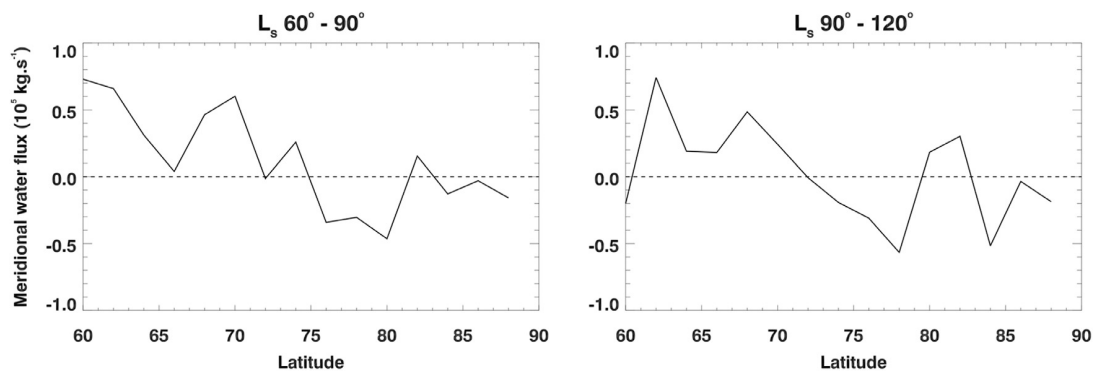


Fig. 13. MarsWRF simulation of the latitudinal evolution of the mean meridional water vapor flux (in 10^5 kg.s^{-1}) between $L_s = 60^\circ$ and 120° , using the retrieved CRISM water vapor abundance over the NPR, averaged over the observed Martian years. The southward transport is negative.

The results are presented in Fig. 13. Negative (positive) values of meridional water vapor flux represent net southward (northward) flux of water vapor. In late northern spring ($L_s = 60^\circ - 90^\circ$), the bulk of the southward transport is occurring in the $75^\circ - 80^\circ\text{N}$ latitude band, which closely tracks the location where the highest column water vapor values are occurring in that season (e.g., Figs. 8 and 12). This area of southward water vapor transport moves northward with season, with a secondary peak of southward water vapor transport near $82^\circ - 85^\circ\text{N}$ at $L_s = 90^\circ - 120^\circ$.

The values presented in Fig. 13 are comparable to previous calculations of water vapor flux from other GCMs (e.g., Montmessin et al., 2017) showing typical values of $0.1 - 0.5 \times 10^5 \text{ kg/s}$. Interestingly, the data in Fig. 13 suggests that the water vapor annulus seen here and by Pankine et al. (2010) and others may be a result of convergence of water vapor from both the south and north along the retreating edge of the NPC. Fig. 13 suggests generally northward flux of water vapor south of $70^\circ - 75^\circ\text{N}$ with southward flux to the north side of this latitude. This

would serve to concentrate high values of water vapor in this band.

5. Summary

The extended record over 5 + Martian years (MY 28–MY 33) of observations with the MRO/CRISM yields valuable information that help characterize the water cycle over the north polar cap, the major source of water vapor in the atmosphere of Mars during its northern spring and summer.

The retrieved water vapor column abundances over the north polar region presented here are conducted with a modified version of the radiative transfer algorithm in Smith et al. (2009, 2018), which enables retrievals of water vapor using the 1360 nm absorption band in observations showing the spectral signature of surface H_2O ice. This work presents an improvement over previous studies (Smith et al., 2009, 2018; Fedorova et al., 2010; Toigo et al., 2013; Trokhimovskiy et al., 2015) that either excluded observations over the surface ice, or did not

correct for it, allowing the present results to cover the permanent cap, where higher water vapor column abundances are observed.

For most of the observed years, the onset of the water sublimation occurs around $L_s = 30^\circ$, whereas the peak of the summertime maximum occurs between $L_s = 110^\circ$ and 120° for all the observed years, except for MY30 where it occurred earlier between $L_s = 100^\circ$ and 110° . The maximum column abundance values around the summertime maximum vary between the observed Mars years, with the difference reaching a factor of 1.5 between MY 29 (70 ± 17 pr- μm) and MY 32 (45 ± 10 pr- μm). Later in the season, the water vapor is transported equatorward, and by $L_s = 180^\circ$ at the end of the water deposition period, the water abundance decreases to levels below 10-pr- μm .

The general behavior of water vapor is similar over ice-free and ice-covered surfaces, but lower values of water vapor over ice-covered regions are observed during early spring, followed by a sharp increase during early summer, when the ice-covered regions exhibit rapid sublimation. The retrieved values of water vapor abundance reach 90 ± 22 -pr- μm over the newly exposed water ice from the permanent cap, as compared to 60 ± 15 -pr- μm over the ice-free surfaces that do not extend to the permanent cap. Away from the period around summer time maximum, modest interannual variability in the water vapor abundance is observed within the 25% uncertainty.

Zonal averages of water vapor show a developing water vapor front that occurs at $L_s = 30^\circ$ around 60°N , and then shifts northward with time. The front reaches its maximum intensity around 83°N , and then it starts to dissipate above the permanent cap, before it shifts to lower latitudes, indicating an equatorward transport of water vapor.

A prominent feature during spring between $L_s = 60^\circ$ and 70° shows relatively large levels of water vapor abundance (23 pr- μm). This feature, also reported by Pankine et al. (2010), indicates a water vapor annulus encircling the retreating edge of the seasonal polar cap during spring at latitudes below 75°N . The meridional transport of water we compute here indicate that the annulus may be a result of convergence of water vapor from both south and north along the retreating edge of the NPC.

Future observations with the NOMAD spectrometer on board the ExoMars Trace Gas Orbiter (e.g., Korabiev et al., 2014; Neefs et al., 2015; Vandaele et al., 2015; Patel et al., 2017) will benefit from the high spectral resolving power and the extension of the observing record to more Martian years, thereby giving more constraints on the water cycle over the north polar cap of Mars.

Acknowledgements

The authors acknowledge financial support from the NASA Mars Reconnaissance Orbiter project and are grateful for the work done by the CRISM operations team at the Applied Physics Laboratory who performed all the sequencing and calibration needed to obtain the CRISM data set. Alain Khayat would like to thank Monique Myriam Nasrallah for the insightful discussions and comments during the preparation of this work. The authors wish to thank the anonymous reviewer for the useful remarks and suggestions to improve the manuscript.

References

Appéré, T., et al., 2011. Winter and spring evolution of northern seasonal deposits on Mars from OMEGA on Mars Express. *J. Geophys. Res.* 116.

Berk, A., Bernstein, L.S., Anderson, G.P., et al., 1998. MODTRAN cloud and multiple scattering upgrades with application to AVIRIS. *Remote Sens. Environ.* 65, 367–375.

Brown, A.J., Calvin, W.M., Becerra, P., Byrne, S., 2016. Martian north polar cap summer water cycle. *Icarus* 277, 401–415. <https://doi.org/10.1016/j.icarus.2016.05.007>.

Clancy, R.T., Sandor, B.J., Wolf, M.J., et al., 2000. An intercomparison of ground-based millimeter, MGS TES, and Viking atmospheric temperature measurements: Seasonal and interannual variability of temperatures and dust loading in the global Mars atmosphere. *J. Geophys. Res.* 105, 9553–9572.

Clancy, R.T., Wolff, M.J., Christensen, M.J., 2003. Mars aerosol studies with the MGS-TESS emission phase function observations: Optical depths, particle sizes, and ice cloud

types versus latitude and solar longitude. *J. Geophys. Res.* 108 (E9), 5098. <https://doi.org/10.1029/2003JE002058>.

Christensen, P.R., Anderson, D.L., Chase, S.C., et al., 1992. Thermal Emission Spectrometer Experiment: Mars Observer Mission. *J. Geophys. Res.* 97, 7719–7734.

Davies, D.W., 1982. Water vapor in Mars' arctic: seasonal and spatial variability. *J. Geophys. Res.* 87, 10253–10263.

Fedorova, A., Korabiev, O., Bertaux, J.L., et al., 2006. Mars water vapor abundance from SPICAM IR spectrometer: Seasonal and geographic distributions. *J. Geophys. Res.* 111, E09S08.

Fedorova, A., Trokhimovsky, S., Korabiev, O., Montmessin, F., 2010. Viking observation of water vapor on Mars: Revision from up-to-date spectroscopy and atmospheric models. *Icarus* 208, 156–164. [org/10.1016/j.icarus.2010.01.018](https://doi.org/10.1016/j.icarus.2010.01.018).

Forget, F., Hourdin, F., Fournier, R., Hourdin, C., Talagrand, O., Collins, M., Lewis, S.R., Read, P.L., Huot, J.-P., 1999. Improved general circulation models of the Martian atmosphere from the surface to above 80 km. *J. Geophys. Res.* 104, 24155–24176 (E10) (1999).

Fouchet, T., Lellouch, E., Ignatiev, N.I., et al., 2007. Martian water vapor: Mars Express PFS/LW observations. *Icarus* 190, 32–49.

Haberle, R.M., Jakosky, B.M., 1990. Sublimation and transport of water from the north residual polar cap on Mars. *J. Geophys. Res.* 95, 1423–1437.

Haberle, R.M., Clancy, R.T., Forget, F., Smith, M.D., Zurek, R.W., 2017. The Atmosphere and Climate of Mars. Cambridge University Press <https://doi.org/10.1017/9781139060172>.

Hvidberg, C., Zwally, H., 2003. In: Sublimation of water from the North polar cap on Mars, Workshop Mars Atmosphere Modelling and Observations, Meeting Abstracts, pp. 3.

Jakosky, B.M., Farmer, C.B., 1982. The seasonal and global behavior of water vapor in the Mars atmosphere. *J. Geophys. Res.* 87, 2999–3019.

Jakosky, B.M., Haberle, R.M., 1992. The Seasonal Behavior of Water on Mars. The University of Arizona Press, Tucson, pp. 969–1016.

Khayat, A.S., Villanueva, G.L., Mumma, M.J., Tokunaga, A.T., 2015. A search for SO_2 , H_2S and SO above Tharsis and Syrtis volcanic districts on Mars using ground-based high-resolution submillimeter spectroscopy. *Icarus* 253, 130–141.

Khayat, A.S.J., Villanueva, G.L., Mumma, M.J., Tokunaga, A.T., 2017. A deep search for the release of volcanic gases on Mars using ground-based high-resolution infrared and submillimeter spectroscopy: Sensitive upper limits for OCS and SO_2 . *Icarus* 296, 1–14.

Korabiev, O., Trokhimovsky, A., Grigoriev, A.V., et al., 2014. Three infrared spectrometers, an atmospheric chemistry suite for the ExoMars 2016 trace gas orbiter. *J. Appl. Remote Sens.* <https://doi.org/10.1117/1.JRS.8.084983>.

Lacis, A.A., Oinas, V., 1991. A description of the correlated-k distribution method for modeling nongray gaseous absorption, thermal emission, and multiple scattering in vertically inhomogeneous atmospheres. *J. Geophys. Res.* 96, 9027–9063.

Langevin, Y., Bibring, J.-P., Montmessin, F., et al., 2007. Observations of the south seasonal cap of Mars during recession in 2004–2006 by the OMEGA visible/near-infrared imaging spectrometer on board Mars Express. *J. Geophys. Res.* 112, E08S12.

Maltagliati, L., Titov, D., Encrenaz, T., Melchiorri, R., Forget, F., Keller, H.-U., Bibring, J.-P., 2011. Annual survey of water vapor behavior from the OMEGA mapping spectrometer onboard Mars Express. *Icarus* 213 (2), 480–495.

Maltagliati, L., Montmessin, F., Korabiev, O., Fedorova, A., Forget, F., Määttänen, A., Lefèvre, F., Bertaux, J.-L., 2013. Annual survey of water vapor vertical distribution and water-aerosol coupling in the Martian atmosphere observed by SPICAM/MEX solar occultations. *Icarus* 223 (2), 942–962.

Melchiorri, R., Encrenaz, T., Fouchet, T., Drossart, P., Lellouch, E., Gondet, B., Bibring, J.-P., Langevin, Y., Schmitt, B., Titov, D., Ignatiev, N., 2007. Water vapor mapping on Mars using OMEGA/Mars Express. *Planet. Space Sci.* 55 (3), 333–342.

Montmessin, F., Forget, F., Rannou, P., Cabane, M., Haberle, R.M., 2004. Origin and role of water ice clouds in the Martian water cycle as inferred from a general circulation model. *J. Geophys. Res.* 109 (E10), 2156–2202.

Montmessin, F., Smith, M.D., Langevin, Y., Mellon, M.T., Fedorova, A., 2017. The Water Cycle. In the Book “The Atmosphere and Climate of Mars”. Cambridge University Press <https://doi.org/10.1017/9781139060172>.

Murchie, S., et al., 2007. Compact Reconnaissance Imaging Spectrometer for Mars (CRISM) on Mars Reconnaissance Orbiter (MRO). *J. Geophys. Res.* E05S03, 112. <https://doi.org/10.1029/2006JE002682>.

Neefs, E., Vandaele, A.C., Drummond, R., et al., 2015. NOMAD spectrometer on the ExoMars trace gas orbiter mission: part 1 - design, manufacturing and testing of the infrared channels. *Appl. Opt.* 28, 8494–8520. <https://doi.org/10.1364/AO.54.008494>.

Pankine, A.A., Tamppari, L.K., Smith, M.D., 2009. Water vapor variability in the north polar region of Mars from Viking MAWD and MGS TES datasets. *Icarus* 204, 87–102.

Pankine, A.A., Tamppari, L.K., Smith, M.D., 2010. MGS TES observations of the water vapor above the seasonal and perennial ice caps during northern spring and summer. *Icarus* 210, 58–71.

Patel, M.R., Antoine, P., Mason, J.D., et al., 2017. NOMAD spectrometer on the ExoMars trace gas orbiter mission: part 2-design, manufacturing, and testing of the ultraviolet and visible channel. *Appl. Opt.* 10 (56), 2771–2782. <https://doi.org/10.1364/AO.56.002771>.

Rothman, L.S., 29 colleagues, 2005. The HITRAN 2004 molecular spectroscopic database. *J. Quant. Spectrosc. Radiat. Transf.* 96, 139–204.

Rothman, L.S., 42 colleagues, 2009. The HITRAN 2008 molecular spectroscopic database. *J. Quant. Spectrosc. Radiat. Transf.* 110 (9–10), 533–572.

Rothman, L.S., Gordon, I.E., Babikov, Y., et al., 2013. The HITRAN2012 molecular spectroscopic database. *J. Quant. Spectr. Rad. Transf.* 130, 4–50.

Smith, D.E., et al., 2001. Mars Orbiter Laser Altimeter: Experiment summary after the first year of global mapping of Mars. *J. Geophys. Res.* 106 (E10), 23689–23722. <https://doi.org/10.1029/2000JE001364>.

- Smith, M.D., 2002. The annual cycle of water vapor on Mars as observed by the Thermal Emission Spectrometer. *J. Geophys. Res.* 107, 1–19.
- Smith, M.D., 2004. Interannual variability in TES atmospheric observations of Mars during 1999–2003. *Icarus* 167, 148–165. <http://dx.doi.org/10.1016/j.icarus.2003.09.010>.
- Smith, M.D., 2008. Spacecraft observations of the Martian atmosphere. *Ann. Rev. Earth Plan. Sci.* 36, 191–219. <https://doi.org/10.1146/annurev.earth.36.031207.124334>.
- Smith, M.D., Wolff, M.J., Clancy, R.T., Murchie, S.L., 2009. Compact Reconnaissance Imaging Spectrometer observations of water vapor and carbon monoxide. *J. Geophys. Res.* 114, E00D03. <https://doi.org/10.1029/2008JE003288>.
- Smith, M.D., Daerden, F., Neary, L., Khayat, A., 2018. The climatology of carbon monoxide and water vapor on Mars as observed by CRISM and modeled by the GEM-Mars general circulation model. *Icarus* 301, 117–131. <https://doi.org/10.1016/j.icarus.2017.09.027>.
- Thomas, G.E., Stamnes, K., 1999. *Radiative Transfer in the Atmosphere and Ocean*. Cambridge Univ. Press, Cambridge.
- Tillman, J.E., G., W., 1987. Atmospheric Pressure Point by Point values. VL1 Sols 1-2245 and VL2 Sols 1-1050. Tech. Rep. National Space Sciences Data Center.
- Toigo, A.D., Lee, C., Newman, C.E., Richardson, M.I., 2012. The impact of resolution on the dynamics of the Martian global atmosphere: Varying resolution studies with the MarsWRF GCM. *Icarus* 221 (1), 276–288.
- Toigo, A.D., Smith, M.D., Seelos, F.P., et al., 2013. High spatial and temporal resolution sampling of Martian gas abundances from CRISM spectra. *J. Geophys. Res.* 118, 89–104.
- Trokhimovskiy, A., Fedorova, A., Korablev, O., et al., 2015. Mars' water vapor mapping by the SPICAM IR spectrometer: Five Martian years of observations. *Icarus* 251, 50–64.
- Vandaele, A.C., Neefs, E., Drummond, R., et al., 2015. Science objectives and performances of NOMAD, a spectrometer suite for the ExoMars TGO mission. *Planet. Space Sci.* 119, 233–249.
- Viviano-Beck, C.E., et al., 2014. Revised CRISM spectral parameters and summary products based on the currently detected mineral diversity on Mars. *J. Geophys. Res. Planets* 119, 1403–1431. <https://doi.org/10.1002/2014JE004627>.
- Wolff, M.J., Clancy, R.T., 2003. Constraints on the size of Martian aerosols from Thermal Emission Spectrometer observations. *J. Geophys. Res.* 108, 5097. <http://dx.doi.org/10.1029/2003JE002057>.
- Wolff, M.J., et al., 2006. Constraints on dust aerosols from the Mars Exploration Rovers using MGS overflights and Mini-TES. *J. Geophys. Res.* 111, E12S17. <http://dx.doi.org/10.1029/2006JE002786>.
- Wolff, M.J., et al., 2009. Wavelength dependence of dust aerosol single scattering albedo as observed by the Compact Reconnaissance Imaging Spectrometer. *J. Geophys. Res.* 114, E00D04. <http://dx.doi.org/10.1029/2009JE003350>.
- Zurek, R.W., Smrekar, S.E., 2007. An overview of the Mars Reconnaissance Orbiter (MRO) science mission. *J. Geophys. Res.* 112.